

Article

Validation of Modified Algebraic Model during Transitional Flow in HVAC Duct

Konrad Nering ^{1,*} and Krzysztof Nering ^{2,†}

¹ Faculty of Mechanical Engineering, Cracow University of Technology, 31-864 Cracow, Poland

² Faculty of Civil Engineering, Cracow University of Technology, 31-155 Cracow, Poland; krzysztof.nering@pk.edu.pl

* Correspondence: konrad.nering@pk.edu.pl

† These authors contributed equally to this work.

Abstract: Airflow occurring in a ventilation duct is characterized by low velocity and hence low Reynolds number. In these conditions, either a laminar, transitional or turbulent flow will occur. Different flow conditions result in different values of the friction coefficient. To achieve the transitional flow in numerical simulation, a modified algebraic model for bypass transition (modified $k - \omega$) was used. Numerical simulation was validated using Particle Tracking Velocimetry (PTV) in the circular channel. The modified algebraic model consists of only two partial differential equations, which leads to much faster calculation than the shear stress transport model. Results of the modified algebraic model are largely consistent with either the measurement and shear stress transport model considering laminar and transitional flow. Consistency slightly decreased in turbulent flow in relation to the model using shear stress transport method.

Keywords: steady-state transitional flow; OpenFOAM; numerical simulation; CFD; PTV; HVAC duct



Citation: Nering, K.; Nering, K. Validation of Modified Algebraic Model during Transitional Flow in HVAC Duct. *Energies* **2021**, *14*, 3975. <https://doi.org/10.3390/en14133975>

Academic Editor: Jae-Weon Jeong

Received: 31 May 2021

Accepted: 30 June 2021

Published: 2 July 2021

Publisher's Note: MDPI stays neutral with regard to jurisdictional claims in published maps and institutional affiliations.



Copyright: © 2021 by the authors. Licensee MDPI, Basel, Switzerland. This article is an open access article distributed under the terms and conditions of the Creative Commons Attribution (CC BY) license (<https://creativecommons.org/licenses/by/4.0/>).

1. Introduction

One of the elements of the heat ventilation and air condition (HVAC) system design is to determine the ventilation duct velocity. To achieve this part of design, computational fluid mechanics (CFD) are used [1]. However, CFD in HVAC mainly is used to determine flow parameters in a specific room, not the ventilation duct [2–4]. Airflow velocity in HVAC system is one of the most important parameters of the HVAC system, which determines the comfort of room inhabitants, i.e., thermal comfort [4,5], CO₂ concentration [3]. Flow through HVAC ducting system also consumes energy and it is crucial to balance the comfort and energy consumed by the system, especially when automatic control is applied [6].

In this paper, the authors propose a modified turbulence model applied in CFD simulation to determine the channel velocity profile for model validation by measuring specific velocity profiles in a circular channel with steady flow. Airflow through the ventilation duct characterizes with low velocity [3], which induces low Reynolds Number. At low Reynolds number, the flow can be either laminar, transitional, or turbulent [7,8]. This leads to differences between the flow friction factor and energy losses during the flow through channel. Different friction factor leads also to different heat transfer coefficient [9]. Errors induced by the poor choice of CFD modelling method may have an influence on the simulations of the recuperator, where heat exchange occurs in a gaseous medium.

There are many numerical models to simulate transitional flows available today. There is a set of models based on Reynolds Average Simulation (RAS), models based on Large Eddy Simulation (LES) and Direct Numerical Simulation (DNS). DNS is the most accurate model, but is very time consuming. LES are less accurate but also less time consuming [10]. The fastest are RAS, but its accuracy depends on case. In laminar flow simulations are relatively easy to perform, for turbulent flow when using RAS, there are a set of models that solve turbulence. The most popular turbulence model is $k - \omega SST$ [11]. For simulating

the transitional flow between laminar and turbulent, there is no universal model. The transitional flow can be simulated with, for example, LOTRAN package which is part of the commercial software ANSYS [12]. In the literature, there are comparisons of different RAS models for transitional flow [13]. In the paper, there are results for Spalart-Allmaras, low-Re $k - \epsilon$, Re-Normalisation Group (RNG), Low-Re Shear Stress Transport, $k - \omega$ SST, and V-SA [14] model. The comparisons shows that for transitional flow the best result are obtained with $k - \omega$ SST and V-SA model. Recently, for the transitional flow was proposed modified model based on standard $k - \omega$ [15–17]. The model proposed in [15] was originally developed for turbomachinery, the model from [17] is for flow around airfoils. Only model proposed in [16] which is a modification of [15] model can be applied for internal duct flow, however it was validated only with literature data, not in particular for HVAC ducts. Therefore, in this paper, a validation of this model is performed using PTV measurement method.

The model presented in this work is an algebraic turbulence model based on the standard $k - \omega$ [18,19]. Algebraic model was originally developed in [15]. Because this algebraic model was developed for high Reynolds number flow, a modification proposed in [20] was applied.

To validate the algebraic model used in this work, a measurement using particle tracking velocimetry (PTV) was used. This method is widely used in the measurement of velocity field in fluids and in validate the numerical simulation results [21–25].

2. Governing Equations

The numerical model used in this study for describing statistically steady fluid flow contains a system of partial differential equations. These equations represent the mass and momentum balance. Balance equation system includes the continuity equation and Reynolds-averaged Navier-Stokes equations (RANS) [16]:

$$\frac{\partial u_j}{\partial x_j} = 0, \quad (1)$$

$$\rho \left(\frac{\partial}{\partial x_j} u_j u_i \right) = - \frac{\partial p}{\partial x_i} + \frac{\partial}{\partial x_j} (t_{ij} + \rho \tau_{ij}) \quad i, j = 1, 2, 3. \quad (2)$$

Tensor components t_{ij} and τ_{ij} are determined by:

$$t_{ij} = 2\rho\nu S_{ij}, \quad \rho\tau_{ij} = 2\rho\nu_t S_{ij} - \frac{2}{3}\rho k\delta_{ij}, \quad (3)$$

$$S_{ij} = \frac{1}{2} \left(\frac{\partial u_i}{\partial x_j} + \frac{\partial u_j}{\partial x_i} \right) - \frac{1}{3} \frac{\partial u_k}{\partial x_k} \delta_{ij}. \quad (4)$$

The algebraic turbulence model used for simulation in this study is a modified $k - \omega$ model formulated in [15]. It bases on the standard $k - \omega$ model by Wilcox [18,19]. New model developed in [15] was originally implemented in FLUENT commercial CFD framework. This model introduce factor γ which is a multiplier of the production term in the k -equation. As shown in [15,16,20,26] it enables more accurate description of the flow in the laminar, transitional, and turbulent range. The k and ω equations are defined:

$$\rho \frac{\partial}{\partial x_j} (u_j k) = \rho \gamma \nu_s S^2 - \rho \beta^* k \omega + \rho \frac{\partial}{\partial x_j} \left[\left(\nu + \sigma^* \frac{k}{\omega} \right) \frac{\partial k}{\partial x_j} \right], \quad (5)$$

$$\rho \frac{\partial}{\partial x_j} (u_j \omega) = \rho \alpha \frac{\omega}{k} \nu_s S^2 - \rho \beta \omega^2 + \rho \frac{\partial}{\partial x_j} \left[\left(\nu + \sigma \frac{k}{\omega} \right) \frac{\partial \omega}{\partial x_j} \right] + \rho \frac{\sigma_d}{\omega} \frac{\partial k}{\partial x_j} \frac{\partial \omega}{\partial x_j}, \quad (6)$$

where:

$$v_t = v_s + v_l, \quad v_s = \frac{k_s}{\tilde{\omega}_1}, \quad v_l = \frac{k_l}{\tilde{\omega}_2}, \quad k_s = f_{ss}k, \quad k_l = k - k_s, \quad (7)$$

$$\tilde{\omega}_1 = \max \left[\omega, C_{lim} \frac{\sqrt{2S_{ij}S_{ij}}}{a_1} \right], \quad \tilde{\omega}_2 = \max \left[\omega, C_{lim} \frac{\sqrt{2S_{ij}S_{ij}}}{a_2} \right], \quad (8)$$

$$f_{ss} = \exp \left[- \left(\frac{C_{SS}v\Omega}{k} \right)^2 \right]. \quad (9)$$

The factor γ (intermittency factor) is a multiplier of the production term in k -Equation (5). It is defined as:

$$\gamma = \min \left(\frac{\zeta_T}{A_T}, 1 \right), \quad \zeta_T = \max \left(\frac{\sqrt{k}y}{\nu} - C_T, 0 \right). \quad (10)$$

The intermittency factor γ can be described as a starting function for the turbulence [15]. When $\gamma = 0$ the production term $\rho\gamma\nu_s S^2$ from Equation (5) is also equals to zero. Therefore there is no production of turbulent kinetic energy k , which corresponds with the laminar flow. For the inlet the assumption of $\gamma = 0$ was made. When $0 < \gamma < 1$ production term has non zero which indicates intermittent flow. The values of $\gamma = 1$ leads to fully turbulent flow [16].

Originally, the algebraic intermittency model formulated in [15] was developed to simulate the transition flow in turbomachines. Due to the slightly different flow characteristics in pipes, especially due to different pressure gradient, it was necessary to tune the model constants. As shown in [26], the following model constants shown in Table 1 are suitable for simulating flow in pipes, especially the inlet section where transition phenomena between laminar and turbulent flow occurs. Proposed model is applicable to transient simulations [15], however in terms of research conducted in this paper there is no need to perform time-accurate simulations. It stems from fact that the performed measurements are steady state.

Table 1. Modified constants of algebraic intermittency $k - \omega$ model.

C_T	A_T	C_{SS}	C_{lim}	a_1	a_2	β^*	α	σ	σ^*
15.5	10	6.8	0.875	0.3	0.55	0.09	0.52	0.5	0.6

To compare the results from the algebraic intermittency model, a simulation using $k - \omega$ SST (shear-stress transport) where performed. Formulation of this model was presented in [27,28]. Additional transition equations for intermittency (γ) and transition momentum thickness Reynolds number ($Re_{\theta t}$) are:

$$\frac{\partial(\rho\gamma)}{\partial t} + \frac{\partial(\rho u_i \gamma)}{\partial x_i} = P_{\gamma,1} - E_{\gamma,1} + P_{\gamma,2} - E_{\gamma,2} + \frac{\partial}{\partial x_i} \left[\left(\mu + \frac{\mu_t}{\sigma_\gamma} \right) \frac{\partial \gamma}{\partial x_i} \right], \quad (11)$$

$$\frac{\partial(\rho Re_{\theta t})}{\partial t} + \frac{\partial(\rho u_i Re_{\theta t})}{\partial x_i} = P_{\theta t} + \frac{\partial}{\partial x_i} \left[\sigma_{\theta t} (\mu + \mu_t) \frac{\partial Re_{\theta t}}{\partial x_i} \right]. \quad (12)$$

It was developed for external flows so it has to be adapted for use for internal flows [29]: the constant $c_{\gamma,2}$ form the multiplier of $E_{\gamma,2}$ in the Equation (11), was changed from 50 to 70. Additionally, in the Equation (12), the constant $c_{\theta,t}$, was reduced from 0.03 to 0.015. Original definition of E_γ and P_γ was presented in [28].

3. Numerical Simulations

The presented method and its equations were solved using OpenFOAM (Open-source Field Operation And Manipulation) framework. OpenFOAM can be applied to simulate the condition occurring in HVAC systems [30]. It is open-source software with full access to

the source code, thus facility the implementation of a subordinate models like the modified algebraic intermittency $k - \omega$ turbulence model [16]. The flow domain was a straight pipe with a length of $130D$. To perform the calculation a solver *simpleFoam* was used. All simulations have the same convergence criteria for velocity, pressure, turbulent kinetic energy, and specific dissipation rate, equals to 10^{-4} .

3.1. Mesh

Computational domain was divided into a finite volume with the shape of hexahedra. The mesh was fully parametric with no automatic algorithm applied. To create a mesh suitable for OpenFOAM framework, a tool called *blockMesh* which is part of OpenFOAM was used. The frame of reference and mesh shape (No. 5 according to Tables 2 and 3) were presented in Figure 1.

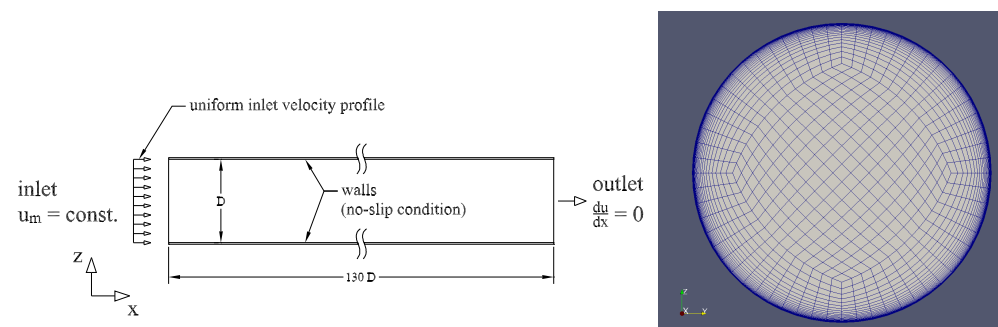


Figure 1. Geometrical model with boundary conditions.

Near the pipe wall, the size of elements was decreased. The y^+ value for a specific flow condition for the mesh No. 5 (according to Tables 2 and 3) were presented in Table 4.

Table 2. Results of τ_w/ρ [m^2/s^2] at the end of simulated duct for different meshes (modified $k - \omega$ model).

Mesh No.	Elements	Re = 630	Re = 1680	Re = 2058	Re = 3108
1	2,340,000	0.0002839	0.0007702	0.00096762	0.00294555
2	3,135,000	0.0002811	0.0007716	0.00102617	0.00221557
3	4,095,000	0.0002799	0.0007740	0.00131656	0.00257593
4	4,788,000	0.0002785	0.0007780	0.00143378	0.00283741
5	5,535,000	0.0002772	0.0007821	0.00145272	0.00288723
6	6,336,000	0.0002772	0.0007888	0.00147504	0.00292444

Table 3. Results of τ_w/ρ [m^2/s^2] at the end of simulated duct for different meshes ($k - \omega$ SST model).

Mesh No.	Elements	Re = 630	Re = 1680	Re = 2058	Re = 3108
1	2,340,000	0.0002871	0.0011365	0.00114578	unstable
2	3,135,000	0.0002869	0.0009390	0.00154990	0.00315847
3	4,095,000	0.0002869	0.0009146	0.00146410	0.00313742
4	4,788,000	0.0002873	0.0008736	0.00138051	0.00302111
5	5,535,000	0.0002873	0.0008679	0.00136535	0.00299605
6	6,336,000	0.0002874	0.0008523	0.00135157	0.00297665

Table 4. Mesh y^+ values.

Re	y^+
630	0.016
1680	0.026
2058	0.036
3108	0.051

To calculate y^+ values, following equation was used:

$$y^+ = \frac{y \cdot \sqrt{\tau_w / \rho}}{\nu}, \quad (13)$$

where τ_w (wall shear stress value) was determined according to the theoretical value of wall shear stress under steady-state conditions at the end of pipe:

$$\tau_w = \Delta p \cdot \frac{D}{4 \cdot L}. \quad (14)$$

where $\Delta p/L$ is a pressure loss according to the Darcy-Weisbach equation. The y length in Equation (13) was the height of the near wall element measured perpendicular to the wall face.

The mesh quality of mesh No. 5 was evaluated using OpenFOAM tool *checkMesh*. Maximum aspect ratio was equalled to 183.787. This value was determined by near wall elements. Maximum mesh skewness equals 0.5907 and the average mesh non-orthogonality was 4.4997. The maximum value of mesh non-orthogonality was 38.573. The mesh consist of 5,535,000 volume elements. To perform mesh independency study different meshes was generated. Result of simulation with these meshes was presented in Tables 2 and 3. The value of steady wall shear stress was picked to show mesh independency [16]. The mesh No. 5 was choose because the relative difference between previous (No. 4) and next (No. 6) mesh according to steady wall shear stress value was less than 2%.

3.2. Boundary Conditions

Simulations were further compared with measurements performed for 4 different Reynolds numbers (Table 4). Reynolds number was defined as following:

$$Re = \frac{u_m \cdot D}{\nu}. \quad (15)$$

The inlet velocity u_m was assumed as uniform at the inlet with a specific turbulence intensity Tu . The inlet turbulence intensity was estimated using correlation in CFD software like FLUENT:

$$Tu = 0.16 \cdot Re^{-0.125}. \quad (16)$$

Turbulent intensity Formula (16) is sufficient for CFD simulations [31] and used for nonturbulent flow in tubes [32,33]. For the laminar flow, there is no need to define the turbulent intensity because the results are independent from Tu values. Therefore, Tu values are only calculated for the Reynolds number where transitional flow is suspected.

Turbulent kinetic energy k and specific dissipation rate ω for the inlet was calculated using following correlations [18]:

$$k = \frac{3}{2}(u_m \cdot Tu)^2, \omega = \frac{\sqrt{k}}{l}, \quad (17)$$

where l is turbulent length scale defined by $l = 0.07 \cdot D$.

For the $k - \omega$ SST turbulence model, an additional boundary condition needs to be applied. The value of $Re_{\theta t}$ at the inlet cross section is calculated using the correlations presented in [34] for $Tu > 1.3$:

$$\text{Re}_{\theta t} = 331.50 \cdot [Tu - 0.5658]^{-0.671} \cdot F(\lambda_{\theta}), \quad (18)$$

where

$$F(\lambda_{\theta}) = 1; \lambda_{\theta} = 0. \quad (19)$$

Estimated $\text{Re}_{\theta t}$ and Tu values for different Reynolds numbers were presented in Table 5. Other boundary conditions were:

- inlet k and ω calculated using inlet turbulence intensity Tu ;
- no slip velocity on walls;
- no wall function for k , ω and v_t fields;
- constant pressure at the outlet;
- no velocity change at the outlet.

Table 5. Flow parameters used in numerical simulations.

Re	Inlet Tu [%]	$\text{Re}_{\theta t}$
1680	6.3	102.4
2058	6.2	104.3
3108	5.9	108.4

4. Experiment Setup

To perform model validation, a measurement using 2-dimensional PTV method was made. Authors decided to measure the velocity profile in one section ($x = 32D$) of the pipe with different Reynolds numbers, because in this section can be observed the greatest change in velocity profile in pipe as pointed in [20,29]. Moreover in this section for Reynolds number $\text{Re} = 630$, the velocity profile was close to parabolic due to laminar flow. For greater Reynolds number, like $\text{Re} = 1680$ and $\text{Re} = 2058$, initial stadium of intermittent flow was observed. While for $\text{Re} = 3108$ starts of the turbulent flow can be seen. Therefore in a specific pipe cross-section ($x = 32D$) with different Reynolds number, it can be observed different types of flow. Measurement setup was presented in Figure 2. In this setup, a laser with regulated pulse frequency and light intensity with a wavelength of 450 nm was used. To control PTV measurement process, the mean velocity was measured using CTA (Constant Temperature Anemometer). The anemometer probe was located in the duct near the end before fan, where the flow conditions are steady.

The CTA measurement was performed using BABUC/A device (manufacturer LSO Lastem s.r.l.) with hot wire anemometric probe BSV101 attached. Specification for BSV101 is given in Table 6.

Temperature of the air in the experiment equals to 24.8 °C and its dynamic viscosity was 1.739×10^{-5} [Pa s].

Table 6. CTA measurement parameters.

Range	0–45 m/s
Accuracy	0–0.5 m/s: ± 5 cm/s 0.5–1.5 m/s: ± 10 cm/s >1.5 m/s: 4%
Response time	10 ms
Resolution	0.01 m/s
Sensing element	platinum wire 18 μm

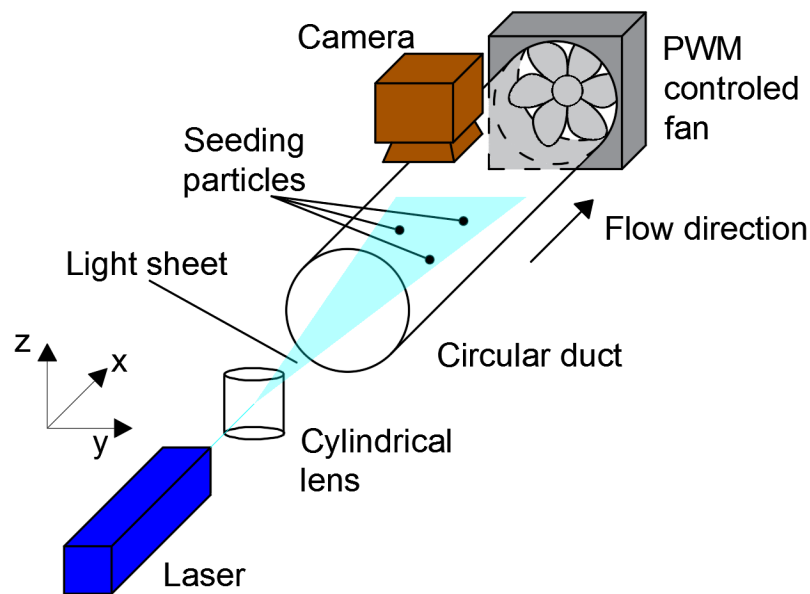


Figure 2. Measurement setup.

4.1. Measurement Method

General principle of the measurements was to obtain the velocity profile inside the tested pipe using PTV single-frame/multiple pulse method [35]. This was achieved by recording the moving particles inside the tested pipe and calculating the mentioned velocity profile based on the distance between given particle locations Δs along the pipe width and known frequency of laser pulse $1/\Delta t$, where Δt is the laser pulse period. This method required low concentration of seeding particles and stable flow conditions during measurement.

4.2. Image Calibration

In order to provide valid values for measured Δs length, proper calibration using image scaling in length and height of the measured pipe was conducted. Image distortion due to light refraction through the pipe wall and other distortions was also taken into account. It was done by inserting the measure reference plane into the pipe fitted with laser sheet, and making the reference photography as seen in Figure 3 with the same parameters as in the image acquisition process with seeding particles. After obtaining the calibration image the reference plane was removed from the test duct.

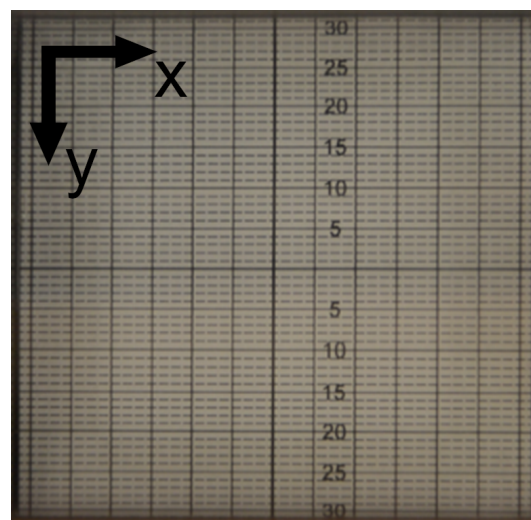


Figure 3. Reference calibration image in pipe middle cross-section.

4.3. Image Processing

Image acquisition using PTV method was conducted by recording a movie with a duration of 60 s with 25 frames per second. Exposure time for each frame was equal to frame duration. Shutter setting was set to provide proper visibility of the tracked particles without the occurrence of motion blur of the recorded particles. Recording method was presented in Figure 4.

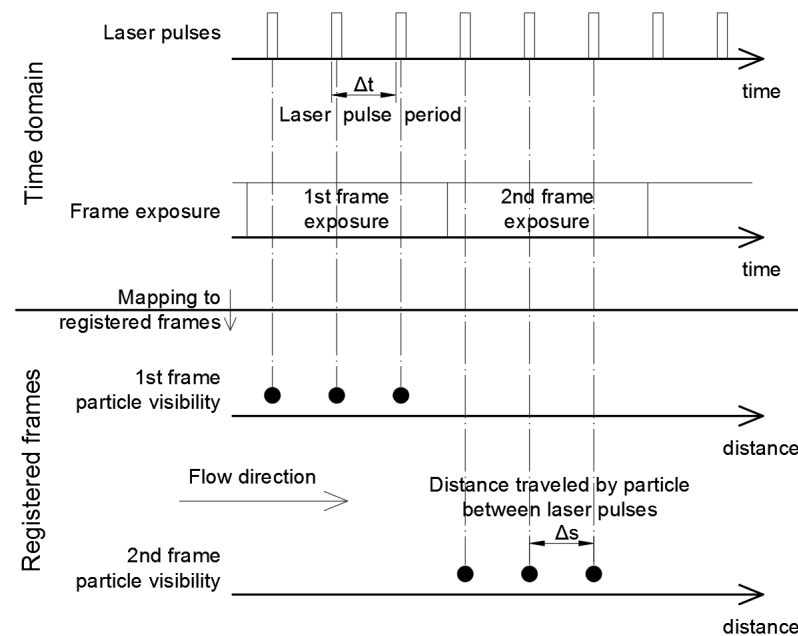


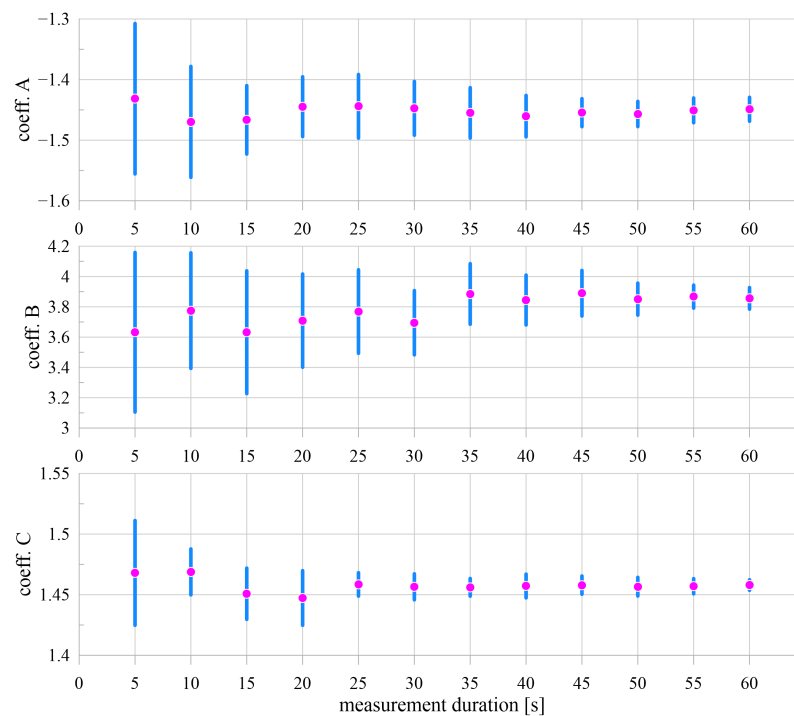
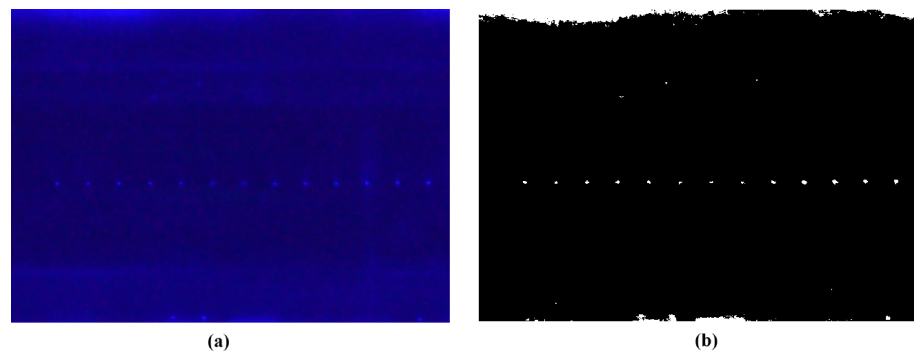
Figure 4. Principle of image processing during the measurement.

Value of 25 frames per second is dictated by the fact that in the measurement procedure Δs (which is the distance of a single particle travelled between the subsequent lasers pulses) is registered (as presented in Figure 4). Increase in frame exposure, thus a decrease in frame rate to 25 frames per second gives sufficient quantity in laser pulses—and distinct particle locations. Duration of image acquisition stems from the preliminary analysis of the convergence of coefficients A, B, C for the fitting curve given in Formula (20). The analysis of convergence of A, B, C consisted of 10 measurements of PTV for $Re = 3108$ for each given duration (5 s, 10 s, 15 s, . . . up to minimal duration meeting the requirements) for a fixed value of 25 frames per second. The requirements for this article were assumed to be as follows—average value of the coefficient is varying less than 0.5% two times in a row, the standard deviation value of the coefficient is less than 2% of the average coefficient value two times in a row. Minimal measurement duration is shown in Table 7. The maximum value from the table below resulted in the measurement duration time. Convergence analysis was presented in Figure 5.

Method of recording seeding particle forces to ensure that the laser pulse frequency occurs at least twice during frame exposure. For practical purposes, during measurements the laser frequency was set to a constant value in range 100–400 Hz, so pulses occurred at least four times to avoid mistaking two different particles with a single one within two laser pulses. Exemplary seeding particle registration during measurement was presented in Figure 6.

Table 7. CTA measurement parameters.

Coefficient of Equation (20)	Minimal Measurement Duration [s]		
	A	B	C
Following average value of coefficient is varying less than 0.5% two times in a row	45	60	35
Following standard deviation value is for coefficient is less than 2% of average two times in a row	45	60	35

**Figure 5.** Convergence analysis of A, B, C coefficient (from Equation (20)) using mean value from 10 measurements (dots) with standard deviation (vertical lines) against measurement duration time.**Figure 6.** Seeding particle recorded during the measurement process (a) raw frame image, and (b) frame image with applied threshold filter.

4.4. Seeding Particle Type

Seeding particle diameter used in the measurements presented in this paper was approximately 10 μm . The source of particles used in this measurement was the vapour of glycol triethylene. This size of the particle is good for the measurement type used in this study [36]. The device used for seeding particle was a fog generator Antari model F-80Z (with 0.7 kW heater) which heat up glycol triethylene to generate its vapor.

4.5. Image Analysis and Velocity Profile Calculation

Image analysis was done using MATLAB software. In general, PTV seeding particle localization using single frame/multiple pulse method is done by finding the next positions of seeding particles [35]. In this case, flow is stable and horizontal, method can be simplified as presented below. Threshold filter used in Matlab was built-in function *imbinarize* using adaptive threshold method on image (frame) converted to greyscale. Foreground polarity was set as *bright* to indicate that the foreground is brighter than background and sensitivity was set to manually (0.2–0.4).

After applying the threshold filter, the specific MATLAB script found the seeding particles first position starting from the left side of the analysed frame. The next step was to find the closest similar particle in the horizontal direction, which is in fact the same particle but in different position due to the subsequent laser pulse as described in Figure 4. Knowing the distance between these two particle locations, the next particle location is sought horizontally in the same direction using the previously calculated distance within 10% distance increase. This algorithm is applied for each seeding particle 1st position. After finding a group of particle positions (see Figure 6), the distances between the seeding particle positions were averaged. This method was done for each of the analysed frames (1500 frames in total). It is worth to underline that not every movie frame had a particle registered due to the low concentration of particles.

5. Results and Comparison

To validate the results obtained from model, a comparison with the experiment data was made. Three turbulence model results were presented: modified algebraic $k - \omega$ model, $k - \omega SST$ and standard $k - \omega$ by Wilcox [18,19]. First, to test the model usability steady-state fully-developed turbulent flow was modelled. Results of friction factor λ were presented in Figure 7 with theoretical values of λ for laminar $64/Re$ and turbulent flow using Colebrook formula $(1.8 \times \log_{10} Re - 1.51)^{-2}$ [37].

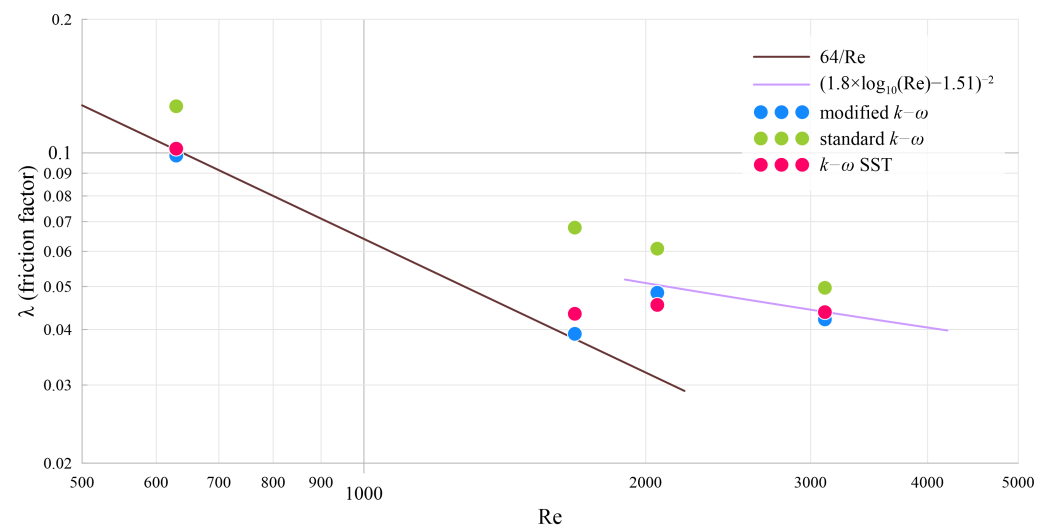


Figure 7. Variation of the fully developed friction factor, λ , for pipe flow.

As seen in Figure 7, standard $k - \omega$ is not suitable for transitional flow at all. However, with higher Reynolds number it gives the correct results. Better fitting is observed for the modified algebraic $k - \omega$ and $k - \omega SST$. Only significant differences but less than 10% are seen in the transitional flow near Reynolds number equals to 2000.

5.1. Model Results

The main purpose of numerical simulation was to obtain the velocity profiles in the specific cross-section of the analysed pipe. The section was located, as mentioned before, in $x = 32D$ from the pipe inlet. In this section, for all four analysed values of the Reynolds

number, different types of flow can be observed. In Figures 8–11 the relative velocity profile (for cross-section $x = 32D$) and relative wall shear stress are shown. Relative velocity is defined as the ratio of absolute velocity to the mean velocity of the flow (u/u_m). While the relative shear stress is obtained by dividing the absolute wall shear stress by shear stress calculated using theoretical friction factor values ($\tau_w/\tau_{wt}(\lambda)$). The theoretical values of the shear stress was calculated using Equation (14).

Results obtained from the standard $k - \omega$ model show unphysical results—it was shown only for reference.

In Figure 8a, the velocity profiles for $k - \omega SST$ and modified $k - \omega$ are similar. Profiles do not reach theoretical values of 2 for laminar flow because in the analysed section the laminar flow is not fully developed. This can be observed from the shear stress curves in Figure 8b.

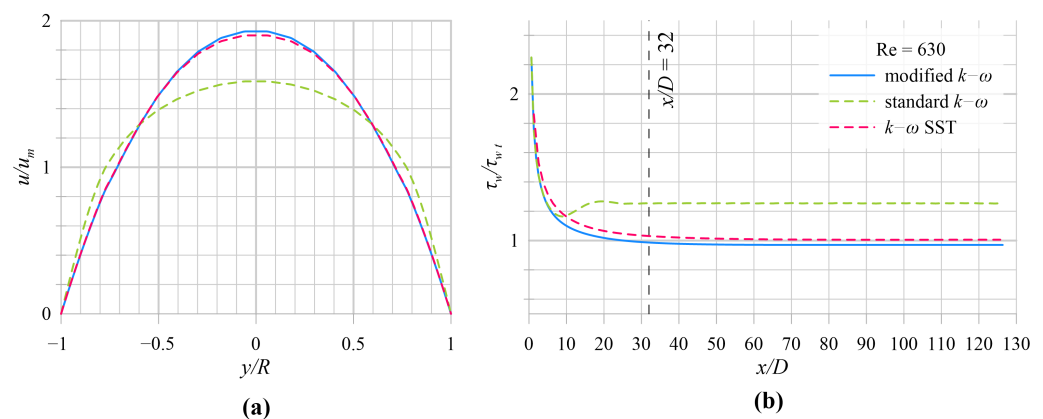


Figure 8. Modelled velocity profile for $x = 32D$ (a) and relative wall shear stress in pipe (b) for $Re = 630$.

In Figure 9a, the velocity profiles start to show intermittent flow but only in the inlet section of pipe. Results from model $k - \omega SST$ and modified $k - \omega$ are similar as previously. Slight difference can be observed in the fully developed flow where $k - \omega SST$ shows increase of wall shear stress due to start of the transitional flow (Figure 9b). Modified $k - \omega$ model still show fully developed laminar flow without observed breakdown.

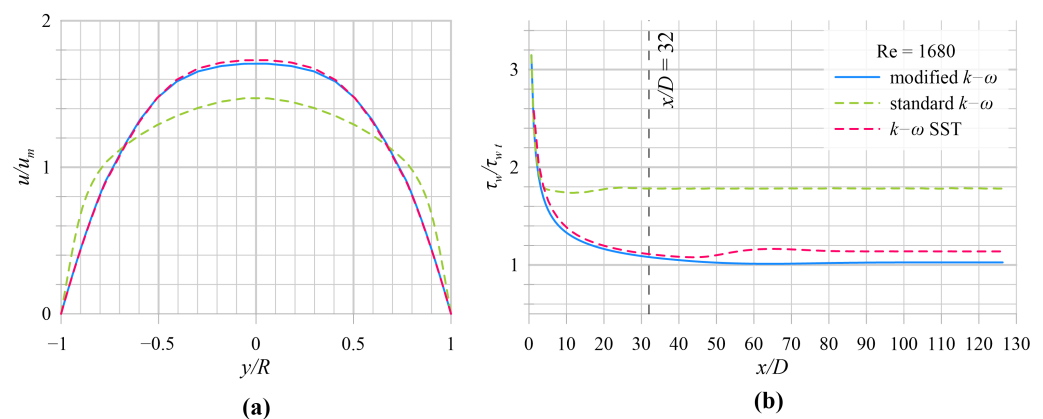


Figure 9. Modelled velocity profile for $x = 32D$ (a) and relative wall shear stress in pipe (b) for $Re = 1680$.

For Reynolds number equals to 2058, the differences between velocity profiles (Figure 10a) from the turbulence model $k - \omega SST$ and modified $k - \omega$ are significant. Laminar breakdown according to wall shear stress profiles (Figure 10b) occurs in section $x \approx 27D$. Extreme values of shear stress between the two models are different but the localisation of breakdown coincide. Shape of wall shear stress results from the modified $k - \omega$ model are

sharper due to the fact of the model formulation—it was also described in [20,26]. For $k - \omega$ SST shape of wall shear stress is compatible with [29]. In a specific cross-section $x = 32D$, the velocity profiles near the wall have different velocity gradient which is correlated with the wall shear stress values.

The last analysis for $Re = 3108$ shows results similar to the previous Reynolds number. Velocity profile differs mainly in the centre of the pipe (Figure 11a), but near the wall the gradient of velocity is similar just like the wall shear stress values presented in Figure 11b. Laminar breakdown location for the modified $k - \omega$ and $k - \omega$ SST model is in the same location near $x \approx 21D$. Moreover the fully developed flows for these models occurs in the approximate region $x \approx 50D$.

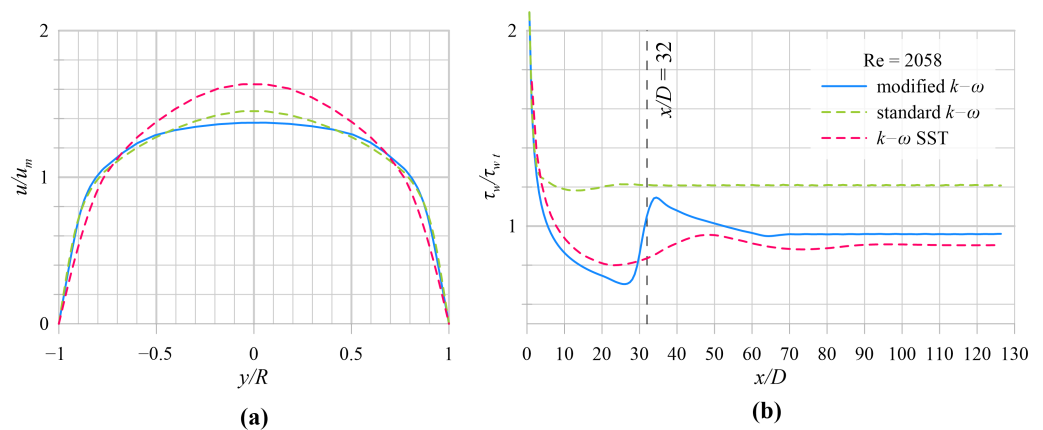


Figure 10. Modelled velocity profile for $x = 32D$ (a) and relative wall shear stress in pipe (b) for $Re = 2058$.

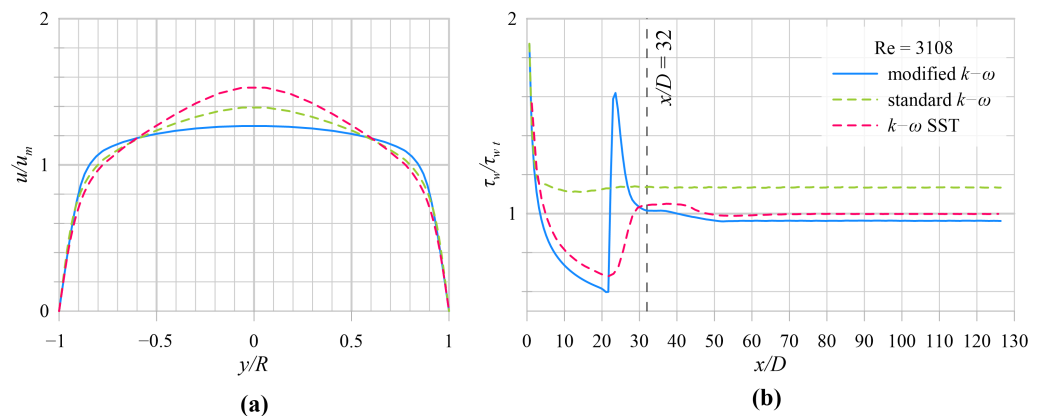


Figure 11. Modelled velocity profile for $x = 32D$ (a) and relative wall shear stress in pipe (b) for $Re = 3108$.

5.2. Experimental Model Validation

To validate the model results, a comparison with PTV measurement values was performed. All velocity profiles were measured in the section at $x = 32D$ of the pipe. Each measurement profile was fitted to a curve based on power law velocity profile [38]:

$$\frac{u}{u_m} \Big|_{FVP} = A \cdot \left(\left| \frac{y}{R} \right| \right)^B + C, \tag{20}$$

where A , B , and C are constants which were obtained during the regression analysis process.

For all Reynolds numbers, the validation of the modified $k - \omega$ model and $k - \omega$ SST was presented in Figures 12–19. In each figure, a plot of error for each measurement point was presented. The error is defined as:

$$E_i = \frac{u_i|_{\text{measurement}}}{u_m} - \frac{u_i|_{\text{model}}}{u_m}. \quad (21)$$

Additionally, an error between the fitted velocity profile (FVP) and model results was presented:

$$E_i^{FVP} = \frac{u}{u_m} \Big|_{FVP} - \frac{u|_{\text{model}}}{u_m}. \quad (22)$$

For $Re = 630$ in Figure 12, the measurement profile (a) with error (b) between measurement and the modified $k - \omega$ model was presented. This is a profile similar to the parabolic velocity distribution for laminar flow as mentioned before. In Figure 13 corresponding analysis for $k - \omega SST$ model was presented. It is worth mentioning that the profile of the standard $k - \omega$ model is not able to describe the laminar flow.

When laminar flows starts to breakdown in the inlet section of the flow for $Re = 1680$ velocity profile for both (modified $k - \omega$ and $k - \omega SST$) models, the velocity profile is flattened in the middle section of the pipe. This is shown in Figure 14a for modified $k - \omega$ and in Figure 15a for $k - \omega SST$. Errors are presented in (b) of corresponding figures.

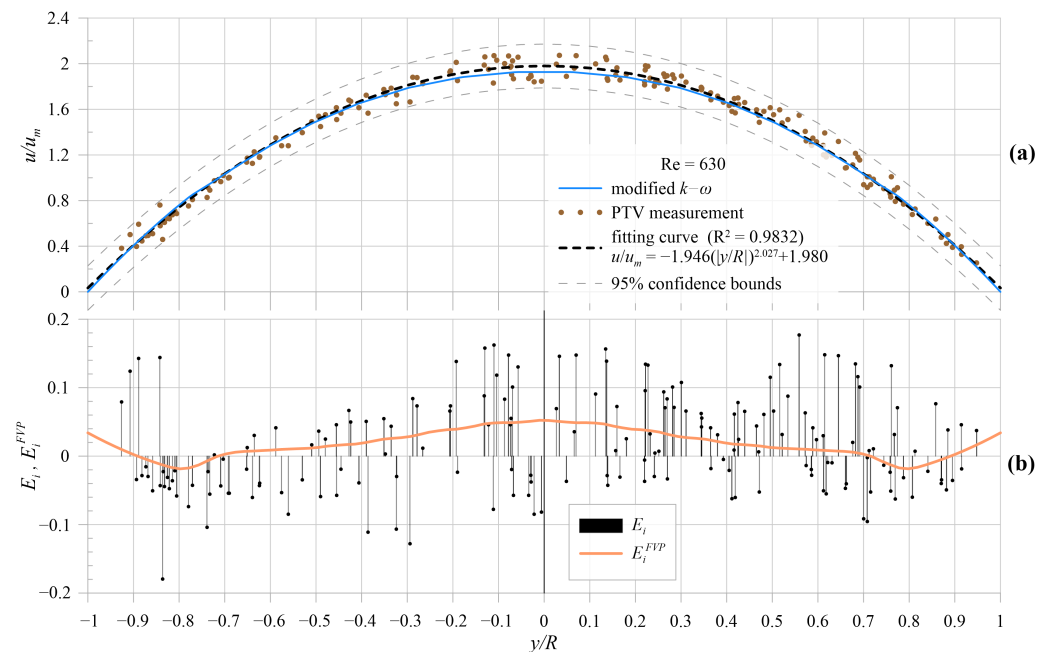


Figure 12. Comparison between PTV measurement and simulation with modified $k - \omega$ model for $Re = 630$ (a) with error values (b).

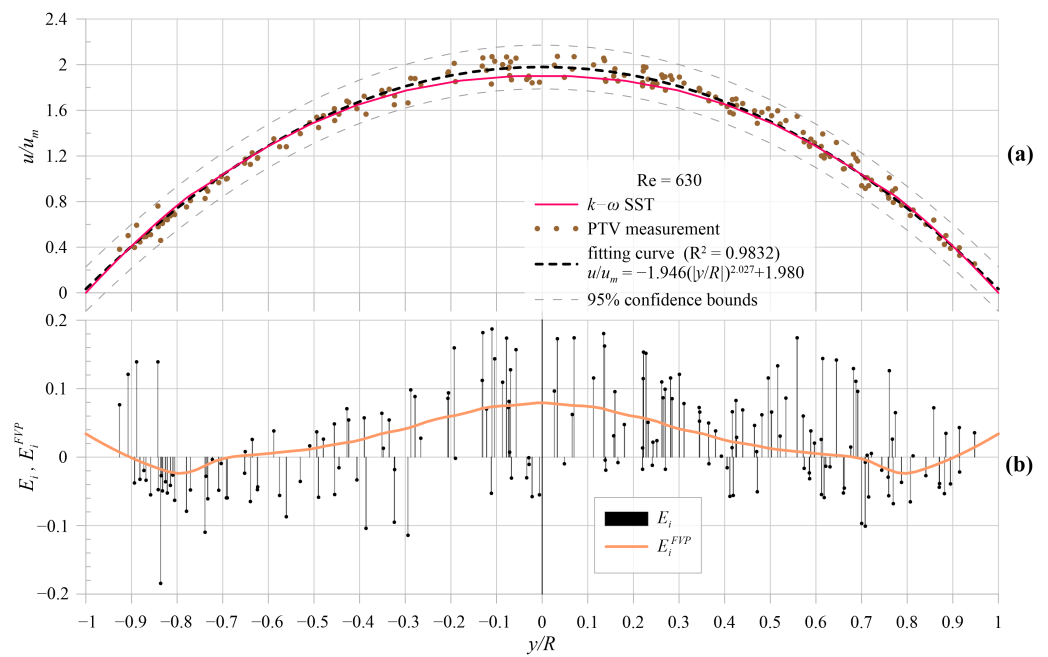


Figure 13. Comparison between PTV measurement and simulation with $k-\omega$ SST model for $Re = 630$ (a) with error values (b).

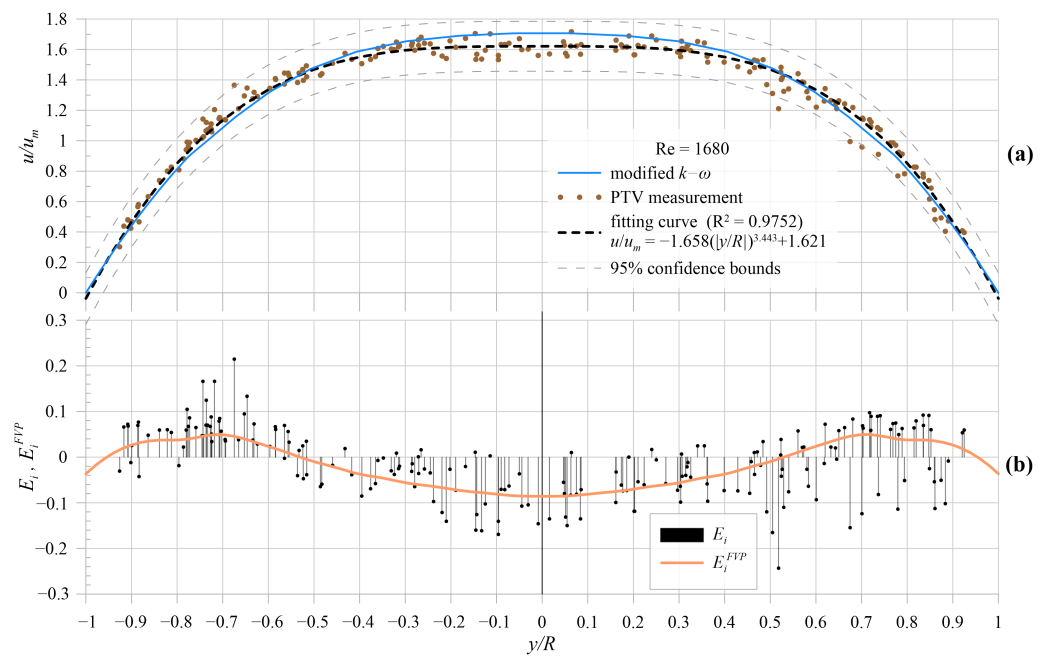


Figure 14. Comparison between PTV measurements and simulations with modified $k-\omega$ model for $Re = 1680$ (a) with error values (b).

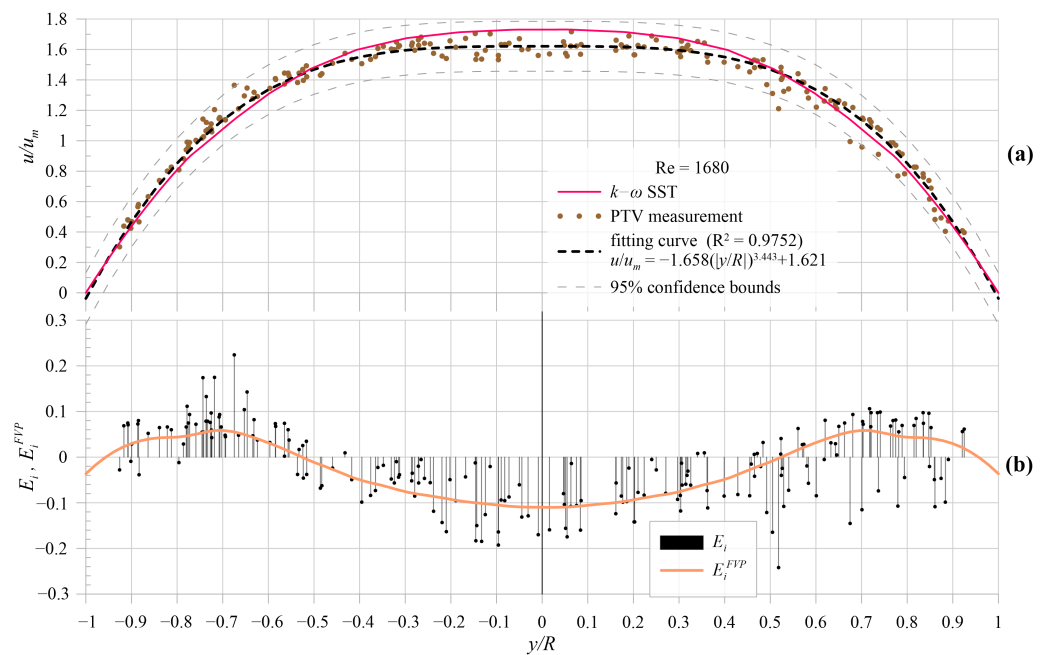


Figure 15. Comparison between PTV measurements and simulations with $k-\omega$ SST model for $Re = 1680$ (a) with error values (b).

For the transitional flow with $Re = 2058$, the modified $k-\omega$ model starts to underestimate the maximum velocity with a slight overestimate of velocity values near wall. This was shown in Figure 16a with error presentation in Figure 16b. The difference between the modified $k-\omega$ model and the measurement could be explained with the rapid increase of wall shear stress near the measured section as shown in Figure 10b. For $k-\omega$ SST analysis of the corresponding Reynolds number, results (a) with errors (b) are shown in Figure 17.

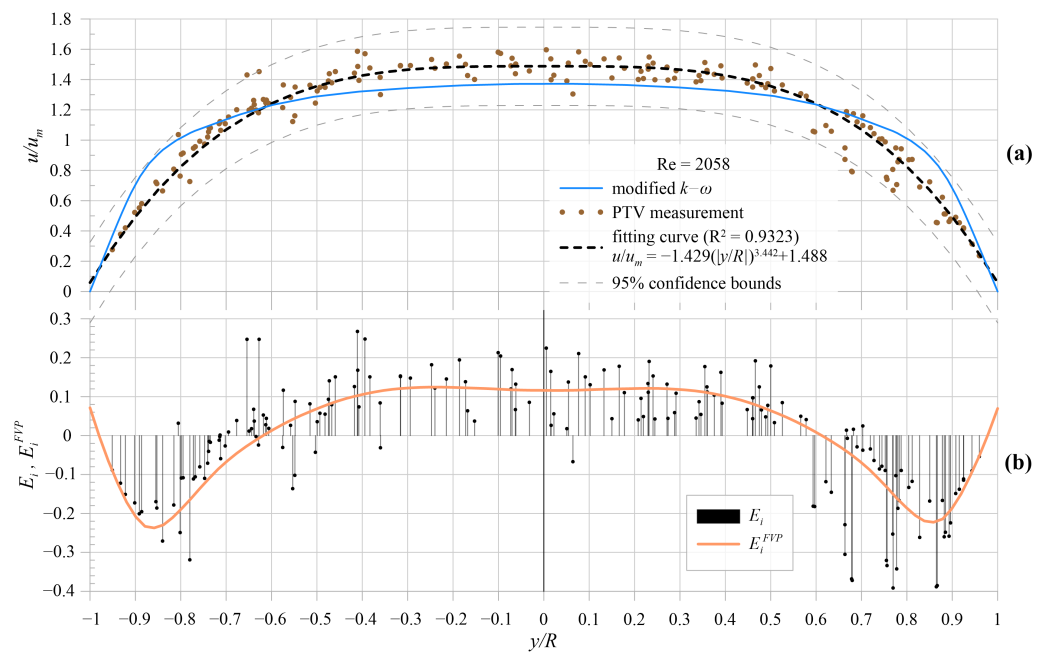


Figure 16. Comparison between PTV measurements and simulations with modified $k-\omega$ model for $Re = 2058$ (a) with error values (b).

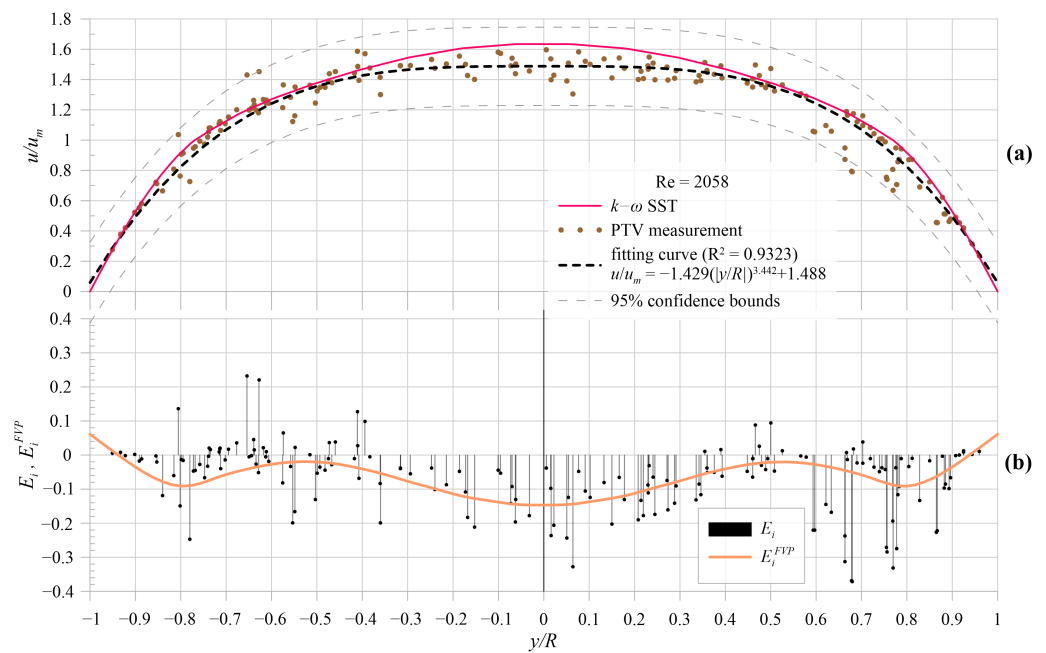


Figure 17. Comparison between PTV measurements and simulations with $k-\omega$ SST model for $Re = 2058$ (a) with error values (b).

For the start of turbulent flow with $Re = 3108$, the modified $k-\omega$ model in the measured section of $x = 32D$ shows an overestimation of velocity values in the middle section of the pipe while increasing the velocity in the near wall section. This was presented in Figure 18a,b where errors are shown. Velocity profile for the fully turbulent flow modelled and its comparison with measurement data was presented in [16]. Results for $k-\omega$ model are presented in Figure 19a,b.

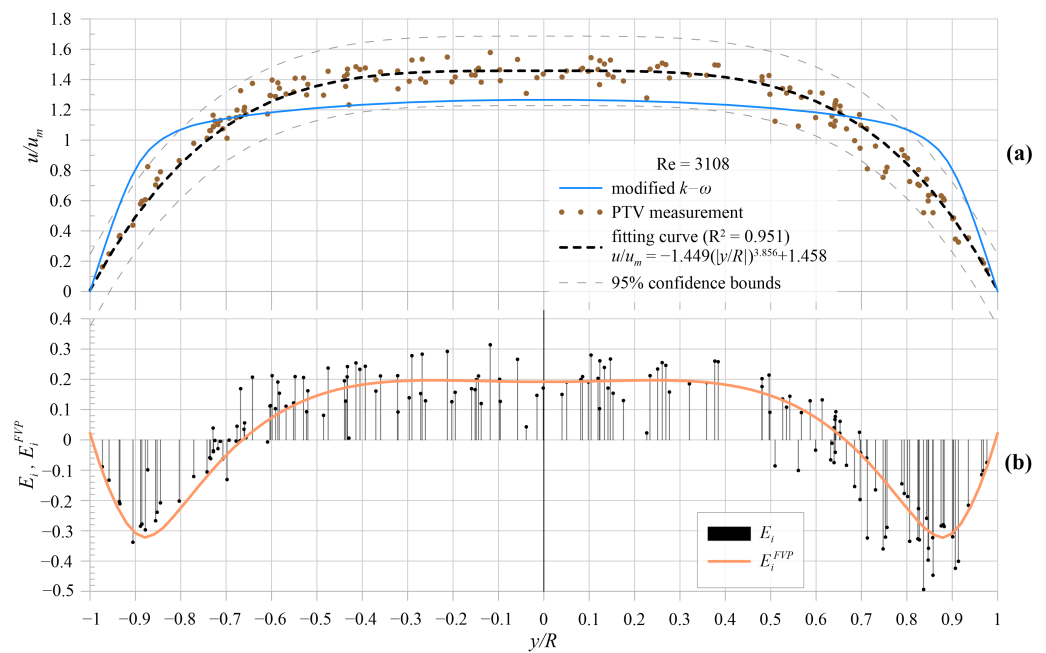


Figure 18. Comparison between PTV measurements and simulations with modified $k-\omega$ model for $Re = 3108$ (a) with error values (b).

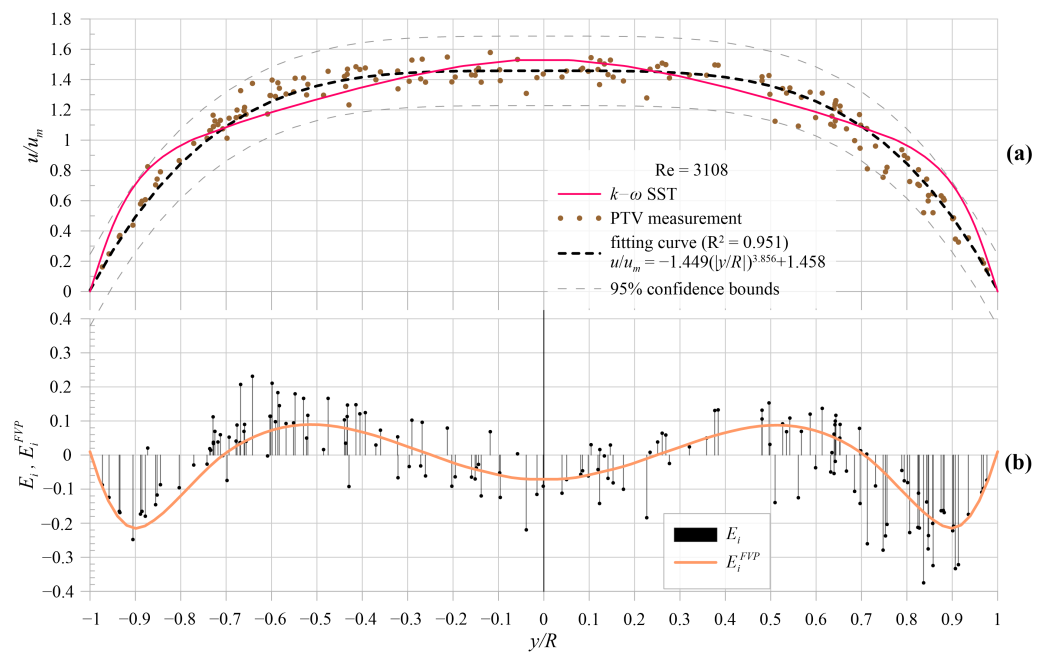


Figure 19. Comparison between PTV measurements and simulations with $k-\omega$ SST model for $Re = 3108$ (a) with error values (b).

To show the goodness of fitting for the model results with measurement, the root mean square error (RMSE) was calculated for each analysis using the following equation:

$$RMSE = \sqrt{\frac{\sum_{i=1}^N E_i^2}{N}}, \quad (23)$$

where N is the number of measurements performed for each condition with the corresponding Reynolds number.

Value of RSME were presented in Table 8.

Table 8. Root Mean Square Error (RMSE) of compared results.

Re	Modified $k-\omega$	$k-\omega$ SST
630	0.072	0.078
1680	0.076	0.086
2058	0.151	0.119
3108	0.199	0.128

6. Discussion and Conclusions

To describe the laminar turbulent transition in the flowing fluid in HVAC circular channel, a modified algebraic model for by-pass transition was adapted. The model was tuned to satisfy the flow conditions specific for pipe flow. Numerical results were compared with the corresponding measurements of air flow through a circular channel using PTV method. Furthermore, the modified $k-\omega$ model was compared with widely used in these types of application model $k-\omega$ SST. The main difference between modified $k-\omega$ and $k-\omega$ SST is the number of equations that solve turbulence. Modified $k-\omega$ consists of standard $k-$ and $\omega-$ equations with algebraic equations for the intermittency factor γ . Model $k-\omega$ SST consists of four partial differential equations for turbulent kinetic energy k , specific dissipation rate ω , intermittency factor γ , and transition momentum thickness Reynolds number $Re_{\theta t}$.

Measurement was performed for specific flow conditions for laminar, transitional, and turbulent flow. Modified $k-\omega$ shows good results in laminar and transitional flow.

For turbulent flow the velocity profile of the model results show slightly higher error than other types of flow. It is due to the fact that the transition area modelled with algebraic model has a rapid change of wall shear stress and velocity profile. However, the location of transition corresponds to the correct values and the steady state fully developed turbulent flow also leads to correct wall shear stress values and correct velocity profile.

One of the advantages of the modified model is its calculation time. In comparison with $k - \omega SST$ simulation with the modified model needs approximately 50% less time to compute. Therefore, designing HVAC systems using the proposed model reduces the need for computing power.

The modified model can also be applied for other flow conditions that appear in HVAC systems - flow-through a pipe heat exchanger where the wall shear stress is crucial because of the dependence on the flow friction factor and heat transfer coefficient. However, the analysis of heat transfer coefficient with transitional flow needs further studies.

Author Contributions: Conceptualization, K.N. (Konrad Nering); methodology, K.N. (Konrad Nering); software, K.N. (Konrad Nering) and K.N. (Krzysztof Nering); validation, K.N. (Konrad Nering) and K.N. (Krzysztof Nering); formal analysis, K.N. (Konrad Nering) and K.N. (Krzysztof Nering); investigation, K.N. (Konrad Nering) and K.N. (Krzysztof Nering); resources, K.N. (Konrad Nering) and K.N. (Krzysztof Nering); data curation, K.N. (Krzysztof Nering); writing—original draft preparation, K.N. (Konrad Nering) and K.N. (Krzysztof Nering); visualization, K.N. (Konrad Nering) and K.N. (Krzysztof Nering); supervision, K.N. (Konrad Nering); project administration, K.N. (Konrad Nering). Both authors have read and agreed to the published version of the manuscript.

Funding: This research received no external funding.

Institutional Review Board Statement: Not applicable.

Informed Consent Statement: Not applicable.

Data Availability Statement: Not applicable.

Conflicts of Interest: The authors declare no conflict of interest.

Nomenclature

k	turbulent kinetic energy [m^2/s^2]
k_l	large-scale turbulent kinetic energy [m^2/s^2]
k_s	small-scale turbulent kinetic energy [m^2/s^2]
Re	Reynolds number [-]
S_{ij}	components of shear rate tensor [1/s]
Tu	turbulence intensity [%]
u	velocity [m/s]
u_m	mean flow velocity [m/s]
y^+	dimensionless wall distance [-]
γ	intermittency factor [-]
ν	fluid kinematic viscosity [m^2/s]
ν_l	large-scale turbulent viscosity [m^2/s]
ν_s	small-scale turbulent viscosity [m^2/s]
ν_t	turbulent viscosity [m^2/s]
ρ	fluid density [kg/m^3]
τ_w	shear stress [Pa]
ω	specific dissipation rate [1/s]
CFD	Computational Fluid Dynamics
FVP	Fitted Velocity Profile
HVAC	Heat, Ventilation, Air Condition
PTV	Particle Tracking Velocimetry
RMSE	Root Mean Square Error

References

1. Shao, L.; Riffat, S. Accuracy of CFD for predicting pressure losses in HVAC duct fittings. *Appl. Energy* **1995**, *51*, 233–248. [[CrossRef](#)]
2. Zhong, W.; Zhang, T.; Tamura, T. CFD Simulation of Convective Heat Transfer on Vernacular Sustainable Architecture: Validation and Application of Methodology. *Sustainability* **2019**, *11*, 4231. [[CrossRef](#)]
3. Ren, C.; Cao, S.J. Development and application of linear ventilation and temperature models for indoor environmental prediction and HVAC systems control. *Sustain. Cities Soc.* **2019**, *51*, 101673. [[CrossRef](#)]
4. Pichurov, G.; Stankov, P.; Markov, D. Hvac control based on CFD analysis of room airflow. *IFAC Proc. Vol.* **2006**, *39*, 213–218. [[CrossRef](#)]
5. Tian, W.; Han, X.; Zuo, W.; Wang, Q.; Fu, Y.; Jin, M. An optimization platform based on coupled indoor environment and HVAC simulation and its application in optimal thermostat placement. *Energy Build.* **2019**, *199*, 342–351. [[CrossRef](#)]
6. Adegbenro, A.; Short, M.; Angione, C. An Integrated Approach to Adaptive Control and Supervisory Optimisation of HVAC Control Systems for Demand Response Applications. *Energies* **2021**, *14*, 2078. [[CrossRef](#)]
7. Taler, D. Determining velocity and friction factor for turbulent flow in smooth tubes. *Int. J. Therm. Sci.* **2016**, *105*, 109–122. [[CrossRef](#)]
8. Abraham, J.; Sparrow, E.; Tong, J. Heat transfer in all pipe flow regimes: Laminar, transitional/intermittent, and turbulent. *Int. J. Heat Mass Transf.* **2009**, *52*, 557–563. [[CrossRef](#)]
9. Rup, K.; Duda, P.; Danys, L. Determination of heat transfer coefficients on the surfaces of plastic tubes. *Heat Mass Transf.* **2002**, *39*, 89–95. [[CrossRef](#)]
10. Fernando, N.; Narayana, M. Limiting value of Reynolds Averaged Simulation in numerical prediction of flow over NACA4415 airfoil. In Proceedings of the 2016 Moratuwa Engineering Research Conference (MERCon), Moratuwa, Sri Lanka, 5–6 April 2016. [[CrossRef](#)]
11. Boiko, A.V.; Demyanko, K.V.; Inozemtsev, A.A.; Kirilovskiy, S.V.; Nechepurenko, Y.M.; Paduchev, A.P.; Poplavskaya, T.V. Determination of the laminar-turbulent transition location in numerical simulations of subsonic and transonic flows past a flat plate. *Thermophys. Aeromech.* **2019**, *26*, 629–637. [[CrossRef](#)]
12. Kirilovskiy, S.V.; Boiko, A.V.; Demyanko, K.V.; Ivanov, A.V.; Nechepurenko, Y.M.; Poplavskaya, T.V. Numerical simulation of the laminar-turbulent transition on a swept wing in a subsonic flow. *J. Phys. Conf. Ser.* **2019**, *1359*, 012070. [[CrossRef](#)]
13. Abdollahzadeh, M.; Esmailpour, M.; Vizinho, R.; Younesi, A.; Páscoa, J. Assessment of RANS turbulence models for numerical study of laminar-turbulent transition in convection heat transfer. *Int. J. Heat Mass Transf.* **2017**, *115*, 1288–1308. [[CrossRef](#)]
14. Vizinho, R.; Páscoa, J.; Silvestre, M. Turbulent transition modeling through mechanical considerations. *Appl. Math. Comput.* **2015**, *269*, 308–325. [[CrossRef](#)]
15. Kubacki, S.; Dick, E. An algebraic model for bypass transition in turbomachinery boundary layer flows. *Int. J. Heat Fluid Flow* **2016**, *58*, 68–83. [[CrossRef](#)]
16. Nering, K.; Rup, K. An improved algebraic model for bypass transition for calculation of transitional flow in parallel-plate channel. *Int. J. Therm. Sci.* **2019**, *135*, 471–477. [[CrossRef](#)]
17. Bernardos, L.; Richez, F.; Gleize, V.; Gerolymos, G.A. Algebraic Nonlocal Transition Modeling of Laminar Separation Bubbles Using $k-\omega$ Turbulence Models. *AIAA J.* **2019**, *57*, 553–565. [[CrossRef](#)]
18. Wilcox, D. *Turbulence Modeling for CFD*; DCW Industries: La Canada, CA, USA, 2006.
19. Wilcox, D.C. Formulation of the $k-\omega$ Turbulence Model Revisited. *AIAA J.* **2008**, *46*, 2823–2838. [[CrossRef](#)]
20. Nering, K.; Rup, K. Modified algebraic model of laminar-turbulent transition for internal flows. *Int. J. Numer. Methods Heat Fluid Flow* **2019**, *30*, 1743–1753. [[CrossRef](#)]
21. You, H.; Tinoco, R.O. Quantifying the Response of Grass Carp Larvae to Acoustic Stimuli Using Particle-Tracking Velocimetry. *Water* **2021**, *13*, 603. [[CrossRef](#)]
22. Özdemir, O.Ç.; Conahan, J.M.; Müftü, S. Particle Velocimetry, CFD, and the Role of Particle Sphericity in Cold Spray. *Coatings* **2020**, *10*, 1254. [[CrossRef](#)]
23. Wang, R.; Duan, R.; Jia, H. Experimental Validation of Falling Liquid Film Models: Velocity Assumption and Velocity Field Comparison. *Polymers* **2021**, *13*, 1205. [[CrossRef](#)]
24. Yang, T.; Liu, Z.; Chen, Y.; Yu, Y. Real-Time, Inexpensive, and Portable Measurement of Water Surface Velocity through Smartphone. *Water* **2020**, *12*, 3358. [[CrossRef](#)]
25. Ma, J.; Niu, X.; Liu, X.; Wang, Y.; Wen, T.; Zhang, J. Thermal Infrared Imagery Integrated with Terrestrial Laser Scanning and Particle Tracking Velocimetry for Characterization of Landslide Model Failure. *Sensors* **2019**, *20*, 219. [[CrossRef](#)] [[PubMed](#)]
26. Nering, K.; Rup, K. An improved algebraic model for by-pass transition for calculation of transitional flow in pipe and parallel-plate channels. *Therm. Sci.* **2019**, *23*, 1123–1131. [[CrossRef](#)]
27. Menter, F.R.; Langtry, R.B.; Likki, S.R.; Suzen, Y.B.; Huang, P.G.; Völker, S. A Correlation-Based Transition Model Using Local Variables: Part I — Model Formulation. In Proceedings of the ASME Turbo Expo 2004: Power for Land, Sea, and Air, Vienna, Austria, 14–17 June 2004. [[CrossRef](#)]
28. Langtry, R.B.; Menter, F.R.; Likki, S.R.; Suzen, Y.B.; Huang, P.G.; Völker, S. A Correlation-Based Transition Model Using Local Variables—Part II: Test Cases and Industrial Applications. *J. Turbomach.* **2004**, *128*, 423–434. [[CrossRef](#)]

29. Abraham, J.P.; Sparrow, E.M.; Tong, J.C.K. Breakdown of Laminar Pipe Flow into Transitional Intermittency and Subsequent Attainment of Fully Developed Intermittent or Turbulent Flow. *Numer. Heat Transf. Part B Fundam.* **2008**, *54*, 103–115. [[CrossRef](#)]
30. Rabani, M.; Madessa, H.B.; Nord, N. Building Retrofitting through Coupling of Building Energy Simulation-Optimization Tool with CFD and Daylight Programs. *Energies* **2021**, *14*, 2180. [[CrossRef](#)]
31. Russo, F.; Basse, N.T. Scaling of turbulence intensity for low-speed flow in smooth pipes. *Flow Meas. Instrum.* **2016**, *52*, 101–114. [[CrossRef](#)]
32. Badar, A.; Buchholz, R.; Lou, Y.; Ziegler, F. CFD based analysis of flow distribution in a coaxial vacuum tube solar collector with laminar flow conditions. *Int. J. Energy Environ. Eng.* **2012**, *3*, 24. [[CrossRef](#)]
33. García-Guendulain, J.; Riesco-Avila, J.; Elizalde-Blancas, F.; Belman-Flores, J.; Serrano-Arellano, J. Numerical Study on the Effect of Distribution Plates in the Manifolds on the Flow Distribution and Thermal Performance of a Flat Plate Solar Collector. *Energies* **2018**, *11*, 1077. [[CrossRef](#)]
34. Langtry, R. Extending the Gamma-Rethetat Correlation based Transition Model for Crossflow Effects (Invited). In Proceedings of the 45th AIAA Fluid Dynamics Conference, Dallas, TX, USA, 22–26 June 2015. [[CrossRef](#)]
35. Cierpka, C.; Lütke, B.; Kähler, C.J. Higher order multi-frame particle tracking velocimetry. *Exp. Fluids* **2013**, *54*. [[CrossRef](#)]
36. Hadad, T.; Gurka, R. Effects of particle size, concentration and surface coating on turbulent flow properties obtained using PIV/PTV. *Exp. Therm. Fluid Sci.* **2013**, *45*, 203–212. [[CrossRef](#)]
37. Colebrook, C.F. Turbulent flow in pipes, with particular reference to the transition region between the smooth and rough pipe laws. *J. Inst. Civ. Eng.* **1939**, *11*, 133–156. [[CrossRef](#)]
38. Afzal, N.; Seena, A.; Bushra, A. Power Law Velocity Profile in Fully Developed Turbulent Pipe and Channel Flows. *J. Hydraul. Eng.* **2007**, *133*, 1080–1086. [[CrossRef](#)]